Nano Energy 133 (2025) 110511

Contents lists available at ScienceDirect

Nano Energy

journal homepage: www.elsevier.com/locate/nanoen

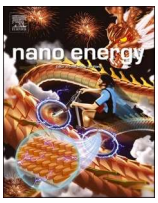

Ultra-sensitive broadband photoresponse realized in epitaxial SnSe/InSe/GaN heterojunction for light adaptive artificial optoelectronic synapses

Yinuo Zhang [a], Lan Li [a], Yunan Lin [a], Xuecen Miao [a], Hong Lei [b], Yi Pan [a,*]

[a] Center for Spintronics and Quantum Systems, State Key Laboratory for Mechanical Behavior of Materials, Xi'an Jiaotong University, Xi'an, Shaanxi 710049, China
[b] Shaanxi Institute for Pediatric Diseases, Xi'an Children's Hospital, Affiliated Children's Hospital of Xi'an Jiaotong University, Xi'an, Shaanxi 710003, China

ARTICLE INFO

Keywords:
SnSe/InSe/GaN heterojunctions
Ultra-low dark current
Broadband photoresponse
Artificial synapses
Light adaptation

ABSTRACT

By integrating sensing, memory, and computing functions within a single unit, the neuromorphic device enables brain-like computing that could facilitate artificial intelligence applications due to its superior scalability and efficiency. As an emerging form of neuromorphic devices, optoelectronic synapses for artificial visual perception with high optical sensing performance and tunable memory time are highly desired. Herein, we report a new design of ultra-sensitive broadband artificial optoelectronic synapses based on a tailored hybrid heterostructure of epitaxial SnSe/InSe/GaN multilayers, in which the interlayer InSe has been employed as the functional layer. Specifically, InSe plays the crucial role of charge trapping layer by blocking the thermally excited carriers in the potential well, thus an ultra-low dark current in 10^{-10} A level has been realized under the bias of −1.5 V. Moreover, the InSe layer could significantly extend the photocurrent decay time, which enabled the synaptic functions in the devices. Such multilayer heterojunctions exhibit a broadband photoresponse spanning from the near-infrared to the ultraviolet, with a specific detectivity up to 1.07×10^{11} Jones under 365 nm excitation. Combining all these merits, light adaptive artificial optoelectronic synapses with multi-color stimuli perception capability have been demonstrated. These results provide a novel and promising strategy for future applications in artificial vision systems.

1. Introduction

The physical separation between the high-speed processing units and low-speed storage units in traditional computer architectures leads to limited computation efficiency and excessive power consumption, which is also known as the von Neumann bottleneck [1–4]. Inspired by the structure and working principle of the biological nervous system, which is superior in speed and energy efficiency, artificial synaptic devices were proposed to realize brain-like parallel information processing. It has been recognized as a promising route toward the next generation tailored high-performance hardware for artificial intelligence [5–10]. In particular, as a special type of synaptic device that is capable of converting optical signals into electrical signals like the human retina, the optoelectronic synapse is showing great potential in the applications of visual perception, in-sensor processing and pattern recognition [11,12]. Owing to their intrinsic advantages of flexibility, scalability and high performance, low-dimensional van der Waals (vdW) materials based devices, such as floating gate nonvolatile memory [2,13,14], memristors [15–17], and phototransistors [18,19], have been reported as candidate units for simulating the synaptic function of the visual system to achieve neuromorphic machine vision.

To simulate the biological visual perception, the function process of the artificial optoelectronic synapses can be decomposed into two aspects, i.e., the front-end optical signal sensing accompanied by instant data preprocessing and the back-end electronic signal transmitting between the units in the brain-like neural networks for memory and learning [20–22]. The optical signal sensing and preprocessing require high sensitivity, responsivity and wavelength-dependent broadband photoresponse, which can be realized by selecting appropriate material and constructing designed heterostructures [21–25]. The memory and effective signal transmission require reasonably long and tunable response time, which is normally achieved by utilizing the charge trapping effects on the photoexcited carriers via defects engineering in the lattice of the channel material [12,26–29]. Additionally, since the illumination at the earth's surface varies by more than 10 orders of magnitude during the day-night cycles, the function of the visual system depends on the ability of the photoreceptors to adjust their sensitivity to the ambient lighting situation, which is realized by the light adaptation

* Corresponding author.
E-mail address: yi.pan@xjtu.edu.cn (Y. Pan).

https://doi.org/10.1016/j.nanoen.2024.110511
Received 19 October 2024; Received in revised form 17 November 2024; Accepted 23 November 2024
Available online 24 November 2024

behavior in human eyes [30]. Therefore, the practical application of artificial optoelectronic synapses in actual scenes also requires environmental adaptivity to the illumination of varying wavelengths and intensity [20,31,32]. As for future industrial applications, since the current exfoliation and transfer process of low-deletional materials is unsuitable for mass production, wafer-scale high-quality materials compatible with semiconductor chip fabrication technology are highly demanded. Although considerable efforts have been devoted to mimicking the visual adaptation of the biological visual system in artificial synapse devices, reliable architectures of the two-dimensional (2D) materials based heterostructure for high-performance artificial optoelectronic synapses which could meet all the requirements are still yet to be fully explored.

In this article, we report light adaptive artificial optoelectronic synapses based on vertical multilayer architecture of tin selenide/indium selenide/gallium nitride (SnSe/InSe/GaN) heterojunction with ultra-sensitive broadband photo-response. The multilayer films are epitaxially grown on GaN(0001) substrates in an ultra-high vacuum (UHV) chamber. The layered vdW semiconductor SnSe has been chosen as the photosensitive layer because of its excellent photoresponse in the visible light (vis) and near-infrared (NIR) range. A thin layer of InSe, which is deliberately sandwiched between the SnSe film and the GaN

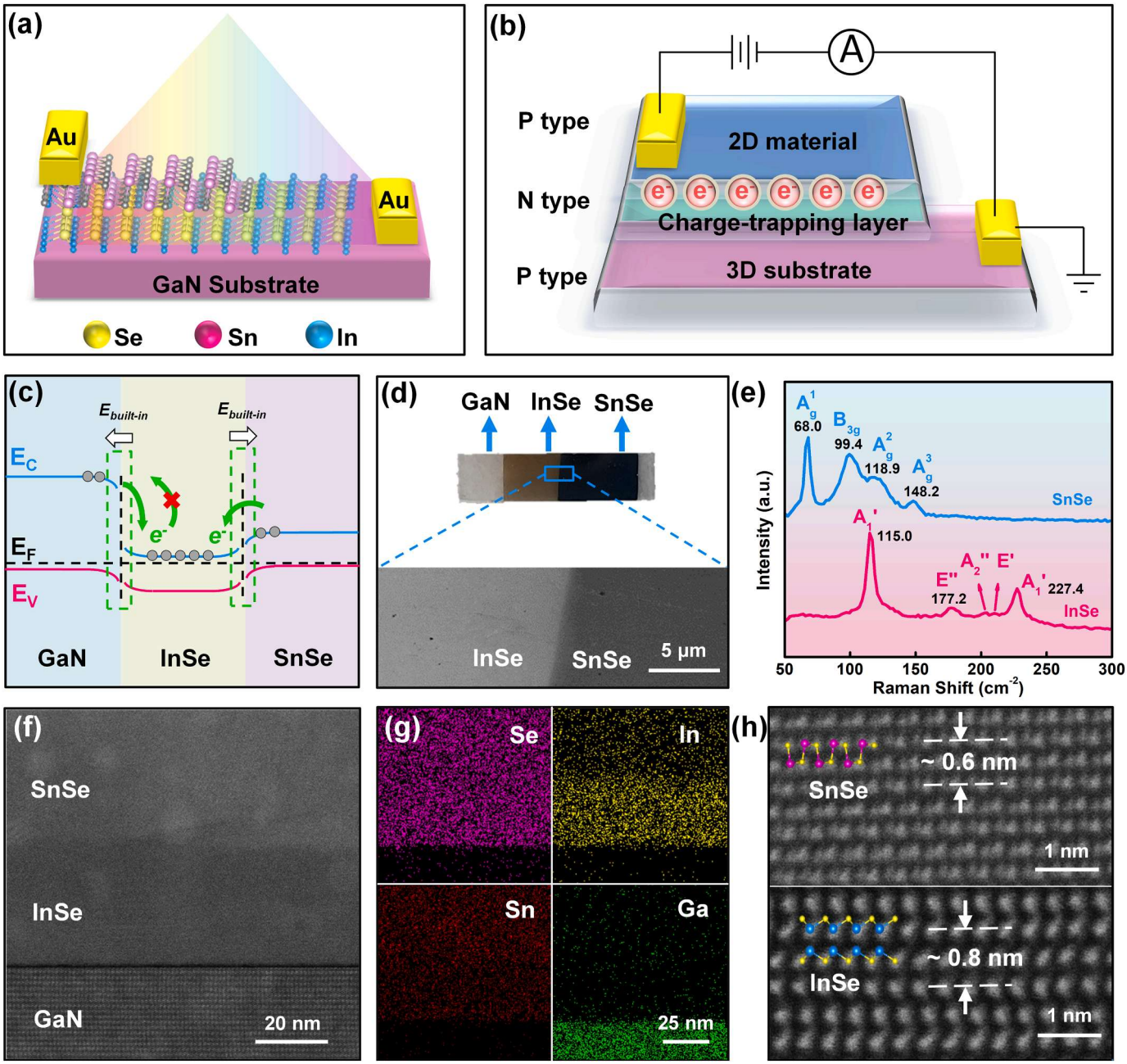

Fig. 1. The structure design, sample growth and characterization of the multilayer heterostructure for broadband photoresponse device. (a-c) Schematic diagrams illustrating (a) the multilayer structures of SnSe/InSe/GaN, (b) Function of the middle layer InSe for charge trapping in the two-terminal device with electrodes attached to the top layer 2D material and 3D substrate, and (c) the charge trapping mechanism of hot electrons confined by the potential well (InSe layer) in the conduction band minimum. (d) Optical microscope (upper panel) and SEM (lower panel) images of the staircase multilayer film with the exposed surfaces indicated by the arrows. Scale bar: 5 μm. (e) Raman spectra taken at the exposed SnSe and InSe regions, respectively. (f) TEM image showing the cross-sectional structure of epitaxial SnSe/InSe layers on GaN(0001) surface, with atomically clean interfaces. (g) EDS mappings showing the element (Se, In, Sn and Ga) distribution in the area corresponding to (f). (h) High-resolution HAADF-STEM image showing the local crystal lattice of the SnSe and InSe layers.

substrate, has been employed as the functional layer to suppress the dark current by blocking the shift of thermally excited carriers. The devices were fabricated by using a shadow-mask-assisted electrode deposition technique in a home-built UHV system. Electrical transport measurements show that the ultra-low dark current in 2×10^{-10} A level could be achieved at room temperature. Optoelectronic measurements reveal broadband photoresponse from ultraviolet (UV) to NIR, with a specific detectivity (D*) up to 1.07×10^{11} Jones for UV. The photoresponse time has been significantly prolonged ($>10^2$) due to the extended photocarrier lifetime originating from the trapping effect of functional layer InSe. Based on these properties, artificial optoelectronic synapses for multi-color stimuli perception have been realized. The synaptic behaviors, like excitatory post-synaptic current (EPSC), pair-pulse facilitation (PPF), and the conversion from short-term plasticity (STP) to long-term plasticity (LTP), have been systematically investigated. Moreover, the light adaptation behavior of such artificial synapses for environmental applications has been simulated by optoelectronic cooperative regulation under variable vis and NIR illumination. This work provides a reliable architecture of 3D-2D hybrid heterojunctions based artificial optoelectronic synapses for large-scale application in energy-efficient neuromorphic machine vision systems in the future.

2. Results and Discussion

2.1. Epitaxial growth of the SnSe/InSe/GaN hybrid heterojunction

Fig. 1a illustrates the designed multilayer van der Waals heterojunction structure, which can be built by vertically stacking P-type SnSe and N-type InSe on P-type GaN(0001) substrate. The top layer SnSe is an intrinsic P-type degenerate semiconductor with a hole concentration of $\approx10^{18}$ cm^{-3} at room temperature. We choose it as the photosensitive layer because of its exceptional photoresponse for vis and NIR range illumination [33–36]. Apart from being the substrate, the GaN also plays a role in extending the photo-response band to the UV range. The middle layer InSe, which is an excellent 2D semiconductor with high electron mobility [37–40], is employed as the functional layer (charge-trapping layer) that could reduce the dark current of the heterojunction-based device (see Fig. 1b) while tuning the photoresponse time. Specifically, it would block the movement of the thermally excited carriers and reduce the dark current of the device. Thus, the sensitivity and dynamic range of the photodetection would be improved even at room temperature.

In order to clarify the mechanism of achieving ultra-low dark current, the energy band diagram multilayer heterojunction is sketched in Fig. 1c. The measured energy bandgap values of GaN, InSe and SnSe are 3.34 eV, 1.27 and 0.95 eV, respectively. These results are obtained by the Tauc plots of UV-NIR absorption spectra (See more details in Note 1 in Supporting Information). A dramatic band offset would occur after contact, giving rise to two back-to-back PN junctions, both in type II band alignment. Considering the different carrier concentrations of P-type GaN, N-type InSe and P-type SnSe, asymmetric depletion regions with two built-in electric fields ($E_{buit\text{-}in}$) in opposite directions are formed. Since the field directions are pointing out on both sides of the InSe middle layer, the flow of the majority carrier (electron) will be blocked. In other words, since a potential well has been formed on the conduction band of the functional layer, the hot carriers will be spontaneously confined there, resulting extremely low dark current [41–45]. In particular, the InSe/GaN heterojunction provides a carrier transmission barrier from narrow bandgap semiconductors to wide bandgap semiconductors, as indicated by the green arrow with red cross in Fig. 1c. This mechanism guarantees a low dark current at the working condition with applied bias on the heterojunction. The type II band structure also plays the role of efficient separation of photogenerated charge carriers, which is essential for high photoresponse performance [46,47].

To realize the designed multilayer structure in high-quality films, the samples are grown by means of physical vapor deposition (PVD) in ultra-high vacuum (see the details in the Experimental Section). As shown in Fig. 1d, the optical microscope (OM) and scanning electron microscope (SEM) images reveal the smooth surface and clear edge of the films. The Raman spectra taken at the exposed SnSe and InSe regions of the film are displayed in Fig. 1e in blue and red curves, respectively. The four main fingerprint peaks of SnSe are all clearly observed at 68, 99.4, 118.9 and 148.2 cm^{-1}, corresponding to the phonon modes of A_g^1, B_{3g}, A_g^2 and A_g^3, respectively [48,49]. The red curve shows five peaks located at 115.0, 177.2, 203.3, 212.3, and 227.4 cm^{-1}, corresponding to the A_1', E′-TO, E", A_2"-LO, and E′-LO Raman modes of gamma phase InSe, respectively [39,48,50]. The clear Raman spectra without extra unknown peaks are evidencing for the high crystallinity and purity of the material. The interfacial information inside the film has been characterized with transmission electron microscopy (TEM) on the specimen cut by focus ion beam in the cross-sectional direction, as shown in Fig. 1f. It displays abrupt interfaces between each layer, suggesting a high-quality heterostructure. It also reveals the layer thickness of InSe is about 32 nm, while top layer SnSe is more than 50 nm, which is optimized to avoid oxidation. The energy dispersive spectroscopy (EDS) mappings showing the element (Se, In, Sn and Ga) distribution in the same area are displayed in Fig. 1g, which confirmed the elemental composition SnSe/InSe/GaN multilayer structure without interdiffusion. The atomic-resolution high-angle annular dark-field (HAADF-STEM) image in Fig. 1h further proves the good crystallinity of SnSe and InSe films. The observed lattice spacing of ~ 0.6 nm and ~ 0.8 nm are consistent with the (101) plane of SnSe and the (100) plane of InSe, respectively. Especially, the cross-sectional image implies the electrical transport direction of the device is along the Sn-Se chains in the (101) plane of the SnSe, which has been proved by early works to be the preferred electron transport direction [51]. These results confirmed the high purity and atomically clean interface of the UHV-grown heterojunctions. These advantages could facilitate stable transport performance of the devices, since the interfacial contamination induced flaws in transport performance, like the hysteretic and transient behaviors, have been avoided.

2.2. Ultra-low dark current and broadband photoresponse realized in SnSe/InSe/GaN devices

The photoresponse performance of the heterojunction has been investigated by measuring the multi-terminal testing devices fabrication on the films. Multiple Au electrodes were deposited on the exposed surface of the SnSe, InSe and GaN region of the staircase multilayer film by utilizing a shadow-mask-assisted electrode deposition technique in a home-built UHV system. Since the device fabrication process was done in situ without exposing the sample surface to air, surface contamination like oxidation and adsorption were strictly avoided. Thus, the clean metal-semiconductor interface guarantees stable ohmic contact of electrodes. The specific device preparation procedure is shown in Fig. S1. The optoelectronic transport measurements of devices were carried out at room temperature in a dark box equipped with fiber lasers and a high-pressure Xe lamp.

To evaluate the suppression effect of the charge trapping layer to the dark current, we compared the transport behaviors of the multilayer heterojunction (SnSe/InSe/GaN) and the simple double-layer heterojunctions (SnSe/InSe and InSe/GaN), as shown in Fig. 2a-c. The current of each type of heterojunction is obtained in dark condition from the corresponding electrodes indicated by inserted device schematics. The dark current values we took for comparison are obtained at the optimized working bias voltage −1.5 V, as indicated by the black arrows. Firstly, the 2D/2D heterojunction of SnSe/InSe shows a high dark current of ~ 10^{-8} A, as displayed in Fig. 2a, implying a poor photoresponse performance with low sensitivity. The thermionic emission dominated high dark current originated from the weak built-in electric field in the SnSe/InSe 2D/2D heterojunction in type II alignment, as shown in Fig. 2d, which allows the diffusion of thermionic electrons in both

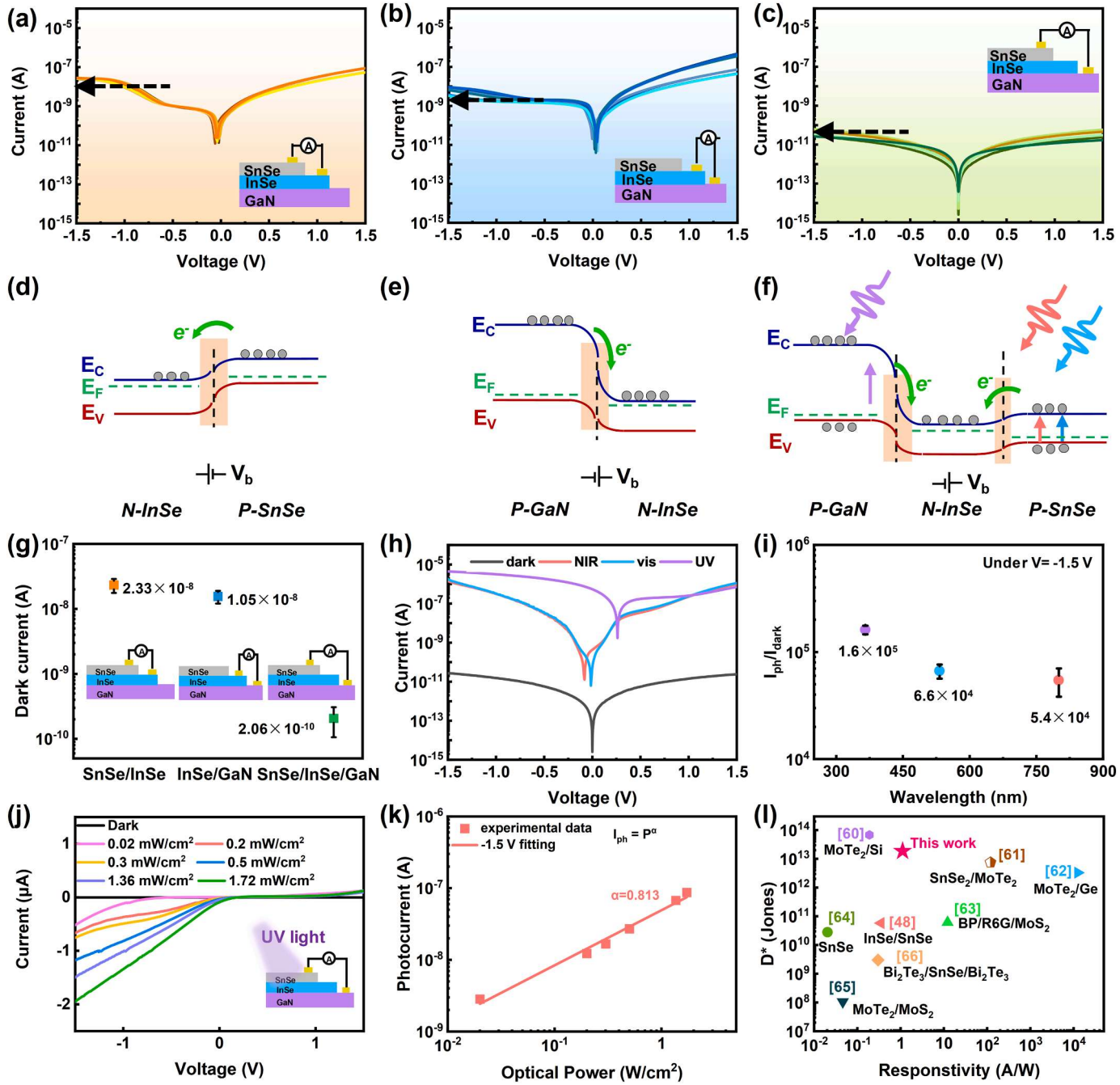

Fig. 2. Optoelectronic transport measurements for the evaluation of dark current and photoresponse performance. (a-c) Representative I-V curves obtained in the dark condition from the corresponding heterojunctions: (a) SnSe/InSe, (b) InSe/GaN, and (c) SnSe/InSe/GaN. (d-f) Schematic energy band diagrams illustrating the photoresponse mechanism of the heterojunctions corresponding to (a-c). Statistical results of the dark current obtained at V = −1.5 V corresponding to the heterostructures in (a-c). (h) I-V curves of the SnSe/InSe/GaN device in the dark condition and under the illumination of varying wavelengths (UV, λ= 365; vis, λ= 532; NIR, λ = 800 nm). (i) The average on/off ratios of photocurrent at V = −1.5 V under NIR, vis, and UV illumination. (j) I-V curves of the SnSe/InSe/GaN device under UV illumination of varying optical power intensities. (k) Linear fitting to the logarithmic plot of photocurrents as a function of illumination power intensity (λ = 365 nm, V = −1.5 V). (l) Comparison of specific detectivity (D*) and responsivity (R) among reported 2D materials photodetectors at room temperature.

directions. Secondly, the 2D/3D heterojunction of InSe/GaN heterojunction shows a reduced dark current of ~ 10^{-8} A level comparing to SnSe/InSe 2D/2D heterojunction, as displayed in Fig. 2b. Such a dark current level is also found in other 2D/3D heterojunctions, like $PtSe_2$/GaN [52] and 2H-$MoTe_2$/Si [53]. A significantly high potential barrier is formed at the InSe/GaN heterojunction, as shown in Fig. 2e, which could reduce the dark current by blocking the back diffusion of thermionic electrons. Thirdly, the current-voltage (I-V) curves of SnSe/InSe/GaN multilayer heterojunction show dramatically suppressed dark currents of ~ 10^{-10} A level at room temperature, as displayed in Fig. 2c, obviously much lower than the SnSe/InSe and InSe/GaN heterojunctions. It is also significantly lower (one order of magnitude) than that of the SnSe/GaN heterojunction (see Fig. S2 in the Supporting Information), which was used as a control group without the InSe middle layer. These results confirmed that the InSe middle layer is playing an important role in reducing the dark current. The mechanism can be explained by the charge-trapping effect of the InSe layer induced potential well at the conduction band minimum, as shown in the band diagram in Fig. 2f. The

band alignment of SnSe/InSe/GaN heterojunction has been experimentally confirmed by the ultraviolet photoelectron spectroscopy (UPS) and UV-NIR absorption spectroscopy measurement (See more details in Note 1 in the Supporting Information). Thus, an ultralow dark 2.06×10^{-10} A can be achieved in the designed SnSe/InSe/GaN multilayer heterojunction, as is revealed by the statistical analysis based on multiple devices, as shown in Fig. 2g. The ultra-high sensitivity would be enabled by the significantly suppressed dark current in the multilayer hybrid heterojunctions fabricated on large-scale epitaxial film, which is essential for the optical stimuli perception of extremely low illumination.

Many other methods have been proposed to reduce the dark current, e.g., introducing an insulating layer [54–56] and interface engineering [57–59]. To compare our work with the recent literature, we listed the results in Table S1(Supporting Information). Compared to the mechanically stacked heterojunctions, the UHV-grown hybrid 2D/3D heterojunction has the advantage of clean interfaces and well-controlled layer thickness in the whole sample. The functional layer thickness has been optimized as 32 nm, which has realized the designed unique band structure and desired performance, i.e., achieving low dark current while avoiding excessive loss of photogenerated carriers. Additionally, the epitaxial growth of the vdW films on GaN substrate is compatible with semiconductor technology, which is favorable for large-scale production.

To further investigate the influence of the functional layer on the optoelectronic properties of the SnSe/InSe/GaN heterojunction, the I-V measurements are carried out under illumination of varying wavelengths (UV: 365 nm, vis: 532 nm and NIR: 800 nm) and incident power density. As shown in Fig. 2h, the I-V curves under constant UV, vis and NIR incident lights reveal broadband photoresponse, which is much higher than those of the InSe/GaN and SnSe/InSe devices (Fig. S4 in the supporting information). The statistical analysis of the on/off ratio (I_{on}/I_{off}) at V = −1.5 V is displayed in Fig. 2i, which shows $(1.6\pm0.15)\times10^5$, $(6.6\pm1.0)\times10^4$ and $(5.4\pm1.6)\times10^4$ for the UV, vis and NIR, respectively. Such a high on/off ratio confirmed the high sensitivity of our multilayer heterojunction devices. Furthermore, the superior room temperature sensitivity allows for a large liner dynamic range with an extended detection minimum threshold, as revealed by the testing results in Fig. 2j, which has been obtained under UV illumination in the power density range of 0.02–1.72 mW/cm^2. Note that the minimum optical power density of 0.02 mW/cm^2 is limited by our light source, it could be further reduced since the photocurrent (0.514 μA) is still much higher than the noise level and the corresponding dark current. The photocurrent can be characterized by the power dependence parameter α, defined by the relation $I_{ph} \propto P^{\alpha}$. Fig. 2k shows the linear fit to the photocurrent I_{ph} as a function of the incident power density at V = −1.5 V. The deduced α value of 0.813 indicates an obviously high photoresponse and large sensitivity for SnSe/InSe/GaN device.

In order to avoid overestimation, the detectivity (D*) can be strictly calculated by considering noise current according to the following Eq. 1:

$$D^* = \frac{\sqrt{A\Delta f}}{NEP} = \frac{\sqrt{A\Delta f}}{i_{noise}/R} \tag{1}$$

where A is the effective device area, Δf is the integration time, i_{noise} is the noise current, and R is the responsivity. Here, it is worth mentioning that the noise current is often replaced by the dark current to calculate the detectivity of photodetectors by $D^* = RA^{1/2}/(2eI_{dark})^{1/2}$, which may result in an overestimated D* and cause some inconsistency in the literature (See more details in Note 2 in the Supporting Information).

We calculated on/off ratio and responsivity (R) under 365 nm illumination (See more details in Note 3 in the Supporting Information). Compared with reported the SnSe and other 2D materials based optoelectronic devices, our device is among the top tier due to ultra-low dark current, as indicated by the red star in Fig. 2l [48,60–66]. The specific values are listed in Table S2 in the supporting Information. The D* of the SnSe/InSe/GaN devices far exceeds that of InSe/GaN devices and SnSe/InSe devices (see Note 4 in supporting information), which confirms the effectiveness of the dual interface strategy in obtaining high-sensitivity devices. These results could meet the requirements of front-end information processing of neuromorphic devices.

Eventually, we can summarize the scenario of the photoresponse process in the SnSe/InSe/GaN device, as schematically illustrated in Fig. 2f. When the device operates under UV illumination, the photoelectrons are generated at the interface between GaN and InSe, then the electrons can be transferred from GaN to InSe by the built-in electric field, lifting the Fermi level of InSe to its valence band. When the negative bias is applied, the built-in electric field at InSe/SnSe interface decreases. The junction diffusion current dominates with the increase of applied negative bias. Therefore, the electrodes on SnSe and GaN can be used to realize UV detection. On the other hand, when the device operates under vis and NIR illumination, the photocarriers are generated at the interface between SnSe and InSe. The generated electron-hole pairs are easily separated by the built-in electric field and collected at the electrodes as photocurrent.

2.3. Artificial optoelectronic synapses for multi-color stimuli perception

Based on the superior broadband photoresponse performance of SnSe/InSe/GaN heterojunction, we designed the two-terminal artificial optoelectronic synapse for multi-color optical stimuli perception, as shown in the left panel of Fig. 3a. Such artificial synapses are inspired by the retina in human eyes, which perceive light stimuli of various colors and convert them into nervous electric signals that can be processed and transmitted through the synapses of neurons. The GaN acts as the presynapse, while the SnSe is employed as the post-synapse. In our design, the synaptic behavior of the device is realized by the InSe functional layer due to the charge trapping induced delay, as illustrated in the right panel of Fig. 3a. We have statistically analyzed the photoresponse time of the original SnSe device and the multi-layer heterojunction device under illumination of various wavelengths (365, 532 and 800 nm), as shown in Fig. 3b. Obviously, the SnSe/InSe/GaN heterojunction shows significantly prolonged ($>10^2$) photoresponse time for all the wavelengths. Thus, the pulsed light induced peaks in the photocurrent could be used to simulate the presynaptic action potential, while the channel conductance between GaN and SnSe is defined as the synaptic weight that can be tuned by the electrical and optical inputs. The presence of InSe interlayer also leads to a longer transport distance, which results in a long transport time. The transport time (τ_t) is determined by the transport distance (L), mobility (μ) and electric field (E) according to Eq. 2: [62,67]

$$\tau_t = \frac{L}{\mu E} \tag{2}$$

A larger τ_t helps to obtain a long carrier lifetime as well as a prolonged photoresponse time of the device (see Fig. S8 in the supporting information), which is crucial for the long-term plasticity in optoelectronic synapse devices. It is worth mentioning that distance (L) can be regulated by controlling the thickness of the InSe film.

For our SnSe/InSe/GaN based synapse, the controllable photoresponse with prolonged decay time enables the device to simulate excitatory synaptic behaviors with EPSC under pulsed illimitation. As shown in Fig. 3c, the EPSC was triggered by applying optical stimuli with wavelengths of 532 nm (optical power: 0.69 mW/cm^2, pulse width: 500 ms, interval time: 10 s). The charges caused by the first optical pulse do not have sufficient time to be incompletely released before the second optical pulse arrives, which originates from the photocarriers trapped in the InSe interlayer. Thus, a further significant increase in current could be acquired. Moreover, the PPF effect can also be indexed as the ratio of the EPSC amplitudes induced by the second and first presynaptic pulses ($A_2/A_1\times100$ %) [21,68], shown in Fig. 3d. It is noted that as Δt decreases from 1650 to 120 ms, the PPF index increases from 18.9 % to

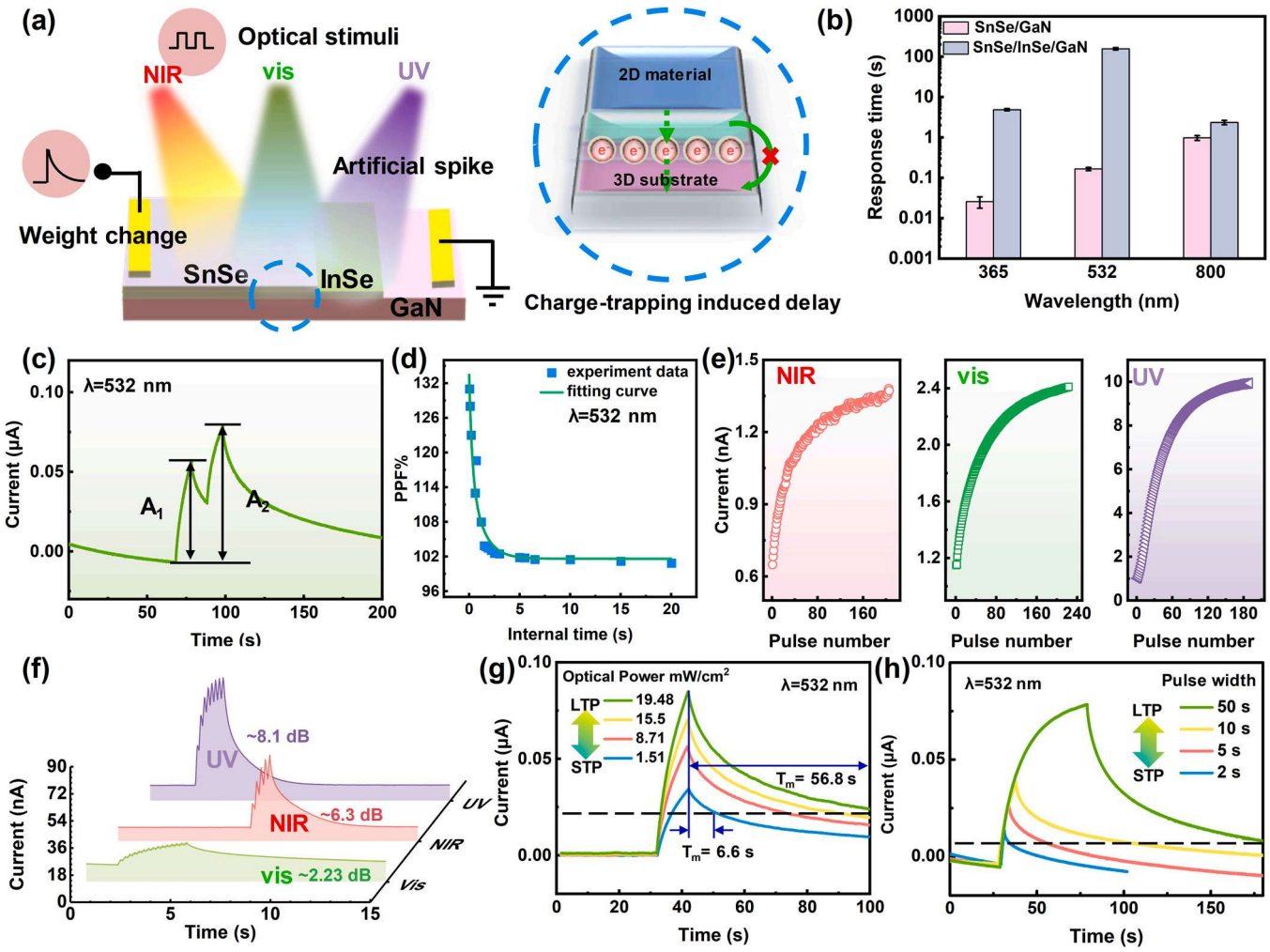

Fig. 3. Synaptic behaviors of SnSe/InSe/GaN based artificial optoelectronic synapse. (a) Left: Schematic diagram of the two-terminal synaptic device with electrodes attached the SnSe and GaN layers, respectively. Right: The dashed circle area showing the charge-trapping induced delay effect of the InSe layer to the photoexcited carriers. (b) Statistical results of decay time (t_{decay}) obtained from the I-t measurements (λ=365 nm, 532 nm and 800 nm) of devices fabricated on SnSe/GaN and SnSe/InSe/GaN. (c) EPSC behavior triggered by two consecutive photonic pulses (532 nm, 0.69 mW/cm^2, 10 s). (d) PPF index as a function of optical pulse interval time Δt. (e) Spike number dependent EPSC of NIR, vis and UV stimulus. (f) EPSC triggered by consecutive pulse series of UV, NIR, and vis illumination, obtained from a SnSe/InSe/GaN artificial synapse. (g, h) Spike intensity dependent EPSC and pulse width dependent EPSC of vis stimulus showing the transition from STP to LTP. T_m is the measured memory time.

61.9 %, as is fitted using the following double-exponential function [20, 69].

$$\text{PPF index} = 1 + B_1 \exp\left(\frac{-\Delta t}{\tau_1}\right) + B_2 \exp\left(\frac{-\Delta t}{\tau_2}\right) \quad (3)$$

Where B_1 and B_2 are the initial facilitation magnitudes, τ_1 and τ_2 are the characteristic decaying time. τ_1 and τ_2 are 66.33 and 333.64 ms, respectively.

Owing to the broadband photoresponse of the device, such PPF and EPSC behavior can also be induced by the 365 nm and 800 nm pulse sequences, as displayed in Fig. S9. Moreover, the EPSC amplitude of the device could be effectively modulated by applying pulse sequences of different wavelengths or pulse numbers, as shown in Fig. 3e. With the increases in pulse number, EPSC amplitude gradually reaches saturation, which is similar to the learning behavior of the human brain [25]. Fig. 3f illustrates the wavelength-dependent postsynaptic currents due to the varying wavelength. Besides, the dynamic ranges (defined by A_n/A_0) [24] were calculated to be ~ 8.1 dB, ~ 6.3 dB, and ~ 2.23 dB for UV, vis and NIR, respectively. This phenomenon can be used to realize color recognition and facilitate the multi-color stimuli perception capability [70].

In the human brain, synaptic plasticity is classified into STP and LTP. While the synaptic plasticity can be transformed from STP to LTP via sustained training activities. This can be achieved in SnSe/InSe/GaN devices by enhancing the light intensity or extending the pulse width. As shown in Fig. 3g, when the light intensity increases from 1.51 mW/cm^2 to 19.48 mW/cm^2, the photocurrent change (ΔIr) is about 0.07 μA, indicating the transition from STP to LTP. The measured memory time (T_m, defined as the time it takes for the photocurrent to decay below the threshold) increases from 6.6 s to 56.83 s (see Fig. S10 in the Supporting Information). It reveals that the memory has been deepened with the increase of learning intensity. After 50 s, 0.02 μA of the sustained photocurrent change (ΔIp) was shown, indicating the rate of forgetting has been delayed as the strength of previous memories increased. Fig. 3h illustrates that as the light duration increases from 2 s to 50 s, the ΔIr of the device improves from 0.01 μA to 0.08 μA, enabling the transition from STP to LTP as well. A similar process can be achieved at 800 nm and 365 nm light conditions in Fig. S11. These results are similar to the learning experience behaviors observed in humans.

Thus, learning and forgetting behaviors of biological synapses can be effectively simulated by the process of applying different wavelengths of light to the device. The learning process of increasing the synaptic

weight is reflected by gradually increased photocurrent under light illumination. The off state of light pulses represents the process of forgetting the previously obtained signals. The required time for the relaxation process could be used to represent the rate of forgetting.

2.4. Light adaptive optoelectronic synapses application

As highlighted in the above discussion, the optoelectronic synaptic plasticity of SnSe/InSe/GaN can be modulated by light power density and the photo response can be adjusted by applying voltage, causing the built-in field can be modulated. Therefore, it is reasonable to speculate that SnSe/InSe/GaN device holds potential for applications in environment-adaptability of light. Specifically, in the human retinal synaptic structure, besides the photoreceptors on the retina, the human pupil can change its size to obtain a comfortable amount of light into the eye, such as strong illumination (sunny), comfortable illumination (cloudy) and weak illumination (night) [71], as shown in Fig. 4a. Taking advantage of the wideband sensing capability of the device, such light adaptation behavior has been realized, light stimulation with the wavelength of 532 nm. Moreover, external voltage-tunable optoelectronic performances have also been realized under the wavelength of 800 nm (> 50 % gain), which is very important for night monitoring vision systems and further application in autopilot vehicles or biomedical engineering [72] [23].

In our device, dazzling illumination, comfortable illumination and weak illumination are simulated by different light intensities applied to the device. Specifically, the light intensity on the device is at the appropriate value (λ= 532 nm, 12.71 mW/cm^2), and the current value falls within the thresholds (upper: 0.075 μA; lower: 0.025 μA), corresponding to a comfortable illumination for the vision, as shown in Fig. 4b. Also, dazzling illumination can sting the eyes. Fig. 4c illustrates the current increases to 0.08 μA, above the upper threshold under 19.48 mW/cm^2. When the light intensity is as low as 2.71 mW/cm^2, the current is below the lower threshold of 0.025 μA (see Fig. 4d), which is similar to impaired vision under weak illumination. To gain appropriate responses within the thresholds for comforable illumination, external bias (V_{ext}) has been set to a lower value, as shown in Fig. 4e. By introducing a negative voltage pulse (-1 V), the current drops below the threshold when dazzling illumination happens, as shown in Fig. 4f. Fig. 4g shows that current within the normal threshold range can be obtained under the same light illumination conditions at a bias of −2.5 V. We further investigate the ability of the external voltage to regulate the current of the photo-synaptic device with a wavelength of 800 nm. The light intensity irradiated on the SnSe/InSe/GaN channel is at an appropriate value of a nA level current under 800 nm at V = −1.5 V, as shown in Fig. 4h. By adjusting the external voltage to −2.5 V, the device obtains μA level current under 800 nm illumination, which indicates the light intensity signal received is over 1.5 times higher. Such light adaptive behavior is closely related to the combined effect of light-modulated photogenerated carrier density and voltage-modulated interfacial barrier. Hence, the SnSe/InSe/GaN device shows promising potential to be employed as an artificial pupil in artificial visual systems within broadband illumination scenarios due to the similar adaptive behavior.

3. Conclusion

In conclusion, we have designed and prepared a vertical vdW multilayer optoelectronic synaptic device based on SnSe/InSe/GaN heterojunction for light adaptive artificial optoelectronic synapses with multi-color perception capability. The devices have reached an ultra-low dark current of 2.06×10^{-10} A and a wide-band optoelectronic response with a detectivity up to 1.07×10^{11} Jones. Therefore, such devices can realize the multifunctional simulation of the human visual system due to the extending carrier life in the multilayer junction. Based on this, the high PPF index and transition from STP to LTP are successfully realized from UV to NIR. In addition, by adjusting the band alignment using different voltages, the artificial retina can adapt to light stimuli with different intensities by modulating the synapses under visible and near-infrared light. Our device provides a novel and promising device design strategy for the large-scale application of artificial vision systems in the future.

4. Materials and methods

4.1. PVD growth of the films

The tin selenide powder (99.999 %, Alfa Aesar) was used as the source material. The freshly GaN (Suzhou Nanowin Science and Technology Co., Ltd, 12 mm × 3 mm) were used as the substrates. Typically, 1 mg of SnSe powder was padded in our home-built evaporator, which is located on a home-built UHV sample stage with two heating wires for substrate heating and evaporation source heating, respectively. Before the growth, both GaN and tin selenide powder need degassing for 30 min at 873 K under 10^{-6} Pa. When depositing material, the GaN substrate is maintained at 573 K, while tin selenide powder is heated to 623 K, and a certain period of vacuum annealing is required after growth. InSe was grown using the same method.

4.2. Characterization of heterojunctions

The sample surface was characterized by an optical microscope (M330–3M180, AOSVI) and an atomic force microscope (Cypher S AFM, OXFORD INSTRUMENTS). The Raman spectra were carried out with a confocal Raman spectrometer (HORIBA) with a 532 nm laser as excitation. The SEM measurement was carried out with a scanning electron microscope (MIRA3-LMH, Tyco Electronics) at 15 KV. The interface structure and elemental mapping analysis were carried out with a TEM (JEM-ARM200F). The SnSe, InSe thin films and GaN substrate were analyzed with Thermo Scientific Xi Using UPS to determine the Fermi level (E_F) and valence level (E_V) of the samples. The gas discharge lamp was used for UPS, with helium gas admitted and the HeI (photon energy 21.22 eV) emission line employed. The light absorption is characterized by UV−NIR absorption spectroscopy (PE Lambda 950).

4.3. Device fabrication

The devices were fabricated within a self-made UHV multi-source physical vapor deposition system under a base pressure lower than 10^{-6} Pa. Au electrodes (50 nm) were directly deposited on the sample surface. We use shadow masks with special patterns to realize the designed patterns. The thickness of electrodes was controlled by using QMS (TMC13, PREAVC).

4.4. Electrical measurements

All device characterizations were measured in a dark box at room temperature, and the data were recorded with a semiconductor characterization system (Keithley 2636B). A high-pressure Xe lamp (CME-SL300, Microenerg) was used as a light source with continuous spectra (wavelength 300–2500 nm), by using filters with different wavelengths to meet the measurement for different bands.

CRediT authorship contribution statement

Lan Li: Validation, Methodology. **Yinuo Zhang:** Writing – original draft, Validation, Investigation, Formal analysis, Data curation. **Xuecen Miao:** Methodology. **Yunan Lin:** Software, Data curation. **Yi Pan:** Writing – review & editing, Writing – original draft, Supervision, Funding acquisition. **Hong Lei:** Writing – review & editing, Supervision.

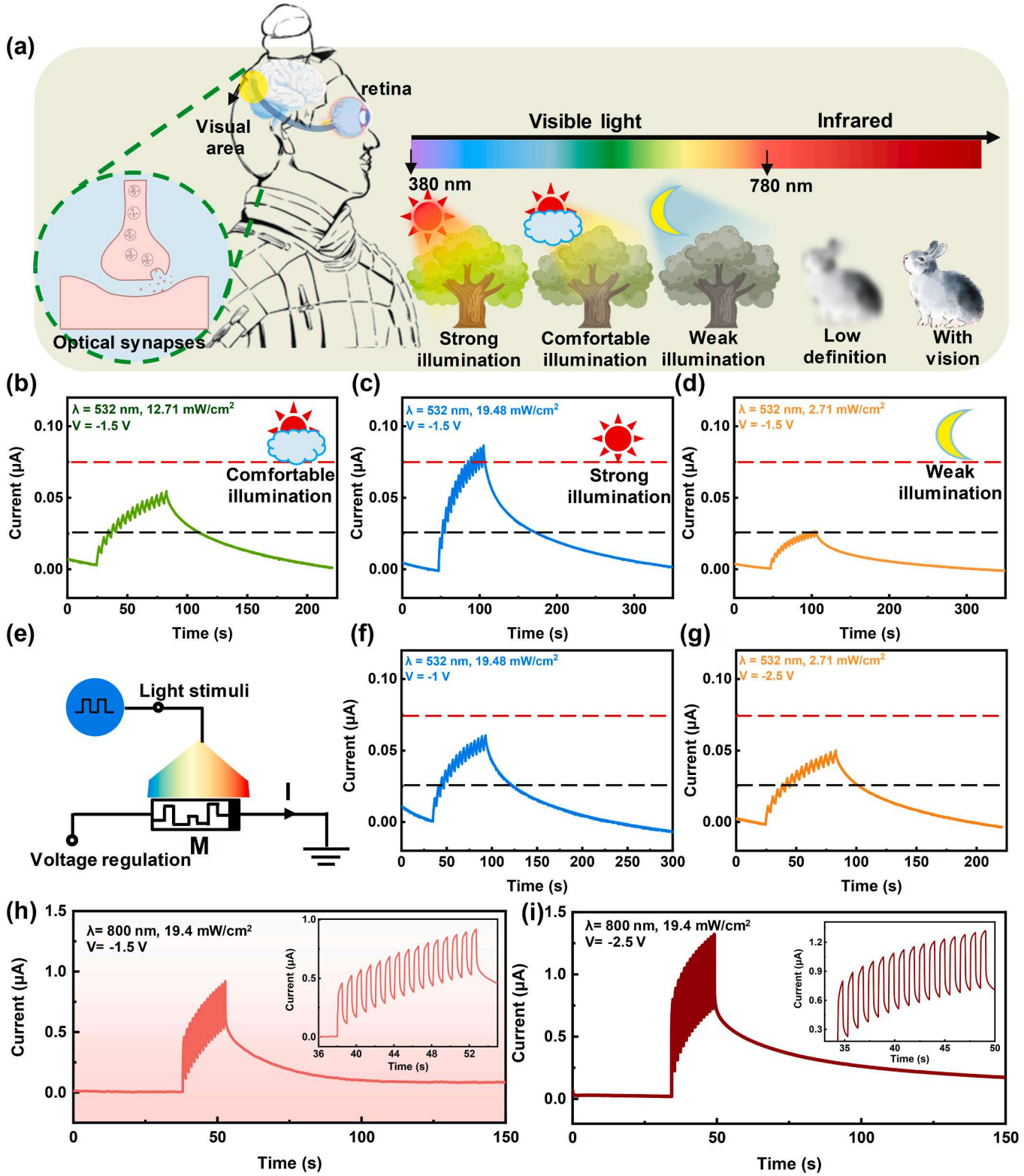

Fig. 4. Simulation of the light adaptation performances of the SnSe/InSe/GaN device. (a) the concept of the device realized adaption behavior under visible light and near-infrared light. (b) The mild light illumination (12.71 mW/cm^2) could not induce injury of human eyes, corresponding to the current that is between the thresholds (upper: 0.075 μA; lower: 0.025 μA). (c) The strong optical stimuli (19.48 mW/cm^2, respectively) with V_{ext} of −1.5 V cause a dazzling visual effect (current above the upper threshold). (d) The weak optical stimuli visual effect (current below the lower threshold). (e) The photocurrent out of thresholds can be tuned back into the comfortable zone by applying appropriate voltage biases. (f) External bias V_{ext} of −1 V for strong illumination and (g) V_{ext} of −2.5 V for weak illumination can be applied to achieve mild stimuli within the thresholds, respectively. (h) Normal V_{ext} of −1.5 V results in ~ 0.9 μA current under infrared stimuli. (i) V_{ext} of −2.5 V results in an increased current of ~ 1.4 μA under the same infrared stimuli.

Declaration of Competing Interest

The authors declare that they have no known competing financial interests or personal relationships that could have appeared to influence the work reported in this paper.

Acknowledgements

This work was financially supported by the National Key Research and Development Program of China (Grant no. 2022YFA1204100) and the National Natural Science Foundation of China (Grant nos. 12074302, 82200728). We thank the Instrument Analysis Center of Xi'an Jiaotong University for their assistance with TEM, Raman, UPS, UV−NIR absorption specetroscopy and SEM measurements.

Supporting Information

Supplementary data associated with this article can be found in the online version.

Appendix A. Supporting information

Supplementary data associated with this article can be found in the online version at doi:10.1016/j.nanoen.2024.110511.

Data Availability

Data will be made available on request.

References

[1] A. Sebastian, M. Le Gallo, R. Khaddam-Aljameh, E. Eleftheriou, Memory devices and applications for in-memory computing, Nat. Nanotechnol. 15 (2020) 529–544.
[2] C. Liu, X. Yan, X. Song, S. Ding, D.W. Zhang, P. Zhou, A semi-floating gate memory based on van der Waals heterostructures for quasi-non-volatile applications, Nat. Nanotechnol. 13 (2018) 404–410.
[3] S. Jiang, S. Nie, Y. He, R. Liu, C. Chen, Q. Wan, Emerging synaptic devices: from two-terminal memristors to multiterminal neuromorphic transistors, Mater. Today Nano 8 (2019) 100059.
[4] H. Li, X. Jiang, W. Ye, H. Zhang, L. Zhou, F. Zhang, D. She, Y. Zhou, S.-T. Han, Fully photon modulated heterostructure for neuromorphic computing, Nano Energy 65 (2019) 104000.
[5] Y. Kim, A. Chortos, W.T. Xu, Y.X. Liu, J.Y. Oh, D. Son, J. Kang, A.M. Foudeh, C. X. Zhu, Y. Lee, S.M. Niu, J. Liu, R. Pfattner, Z.N. Bao, T.W. Lee, A bioinspired flexible organic artificial afferent nerve, Science 360 (2018) 998–1003.
[6] C.A. Brittin, S.J. Cook, D.H. Hall, S.W. Emmons, N. Cohen, A multi-scale brain map derived from whole-brain volumetric reconstructions, Nature 591 (2021) 105–110.
[7] S. Kumar, X. Wang, J.P. Strachan, Y. Yang, W.D. Lu, Dynamical memristors for higher-complexity neuromorphic computing, Nat. Rev. Mater. 7 (2022) 575–591.
[8] Y. Lee, T.-W. Lee, Organic synapses for neuromorphic electronics: from brain-inspired computing to sensorimotor nervetronics, Acc. Chem. Res. 52 (2019) 964–974.
[9] S. Manipatruni, D.E. Nikonov, C.-C. Lin, T.A. Gosavi, H. Liu, B. Prasad, Y.-L. Huang, E. Bonturim, R. Ramesh, I.A. Young, Scalable energy-efficient magnetoelectric spin–orbit logic, Nature 565 (2018) 35–42.
[10] C. Wan, P. Cai, M. Wang, Y. Qian, W. Huang, X. Chen, Artificial sensory memory, Adv. Mater. 32 (2019) 1902434.
[11] T. Ahmed, M. Tahir, M.X. Low, Y. Ren, S.A. Tawfik, E.L.H. Mayes, S. Kuriakose, S. Nawaz, M.J.S. Spencer, H. Chen, M. Bhaskaran, S. Sriram, S. Walia, Fully Light-controlled memory and neuromorphic computation in layered Black Phosphorus, Adv. Mater. 33 (2022) 2004207.
[12] S. Wang, C. Chen, Z. Yu, Y. He, X. Chen, Q. Wan, Y. Shi, D.W. Zhang, H. Zhou, X. Wang, P. Zhou, A MoS2/PTCDA hybrid heterojunction synapse with efficient photoelectric dual modulation and ersatility, Adv. Mater. 31 (2018), 1806227-1806235.
[13] Y. Wang, W. Li, Y. Guo, X. Huang, Z. Luo, S. Wu, H. Wang, J. Chen, X. Li, X. Zhan, H. Wang, A gate-tunable artificial synapse based on vertically assembled van der Waals ferroelectric heterojunction, J. Mater. Sci. Technol. 128 (2022) 239–244.
[14] S. Park, S. Oh, D. Lee, J.H. Park, Ferro-floating memory: Dual-mode ferroelectric floating memory and its application to in-memory computing, InfoMat 4 (2022) e12367.
[15] Z. Cao, B. Sun, G. Zhou, S. Mao, S. Zhu, J. Zhang, C. Ke, Y. Zhao, J. Shao, Memristor-based neural networks: a bridge from device to artificial intelligence, Nanoscale Horiz. 8 (2023) 716–745.
[16] M. Si, Z. Zhang, S.-C. Chang, N. Haratipour, D. Zheng, J. Li, U.E. Avci, P.D. Ye, Asymmetric Metal/α-In_2Se_3/Si crossbar ferroelectric semiconductor junction, ACS Nano 15 (2021) 5689–5695.
[17] B. Lv, W. Xue, Z. Yan, R. Yang, H. Wu, P. Wang, Y. Zhang, J. Hou, W. Zhu, X. Xu, Control of photocurrent and multi-state memory by polar order engineering in 2H-stacked α-In_2Se_3 ferroelectric, Sci. China Mater. 65 (2022) 1639–1645.
[18] K. Xu, W. Jiang, X. Gao, Z. Zhao, T. Low, W. Zhu, Optical control of ferroelectric switching and multifunctional devices based on van der Waals ferroelectric semiconductors, Nanoscale 12 (2020) 23488–23496.
[19] L. Wang, X. Wang, Y. Zhang, R. Li, T. Ma, K. Leng, Z. Chen, I. Abdelwahab, K. P. Loh, Exploring ferroelectric switching in α-In2Se3 for neuromorphic computing, Adv. Funct. Mater. 30 (2020) 2004609.
[20] J. Meng, T. Wang, H. Zhu, L. Ji, W. Bao, P. Zhou, L. Chen, Q.-Q. Sun, D.W. Zhang, Integrated in-sensor computing optoelectronic device for environment-adaptable artificial retina perception application, Nano Lett. 22 (2021) 81–89.
[21] W. Ci, W. Xue, P. Wang, W. Yin, X. Wang, L. Shi, P. Zhou, X. Xu, All-in-one optoelectronic neuristor based on full-vdW two-terminal ferroelectric p–n heterojunction, Adv. Funct. Mater. 34 (2023) 2305822.
[22] P. Feng, S. He, Z. Zeng, C. Dang, M. Li, L. Zhao, D. Wang, L. Gao, Self-powered optoelectronic synaptic devices based on In2Se3/MoS2 ferroelectric heterojunction with boosted performance, Adv. Mater. Technol. 9 (2023) 2301355.
[23] Y. Zhang, B. Wang, Z. Han, X. Shi, N. Zhang, T. Miao, D. Lin, Z. Jiang, M. Liu, H. Guo, J. Zhang, H. Hu, L. Wang, Bidirectional photoresponse in a mixed-dimensional MoS_2/Ge heterostructure and its optic-neural synaptic behavior for colored pattern recognition, ACS Photonics 10 (2023) 1575–1582.
[24] X. Liu, S. Wang, Z. Di, H. Wu, C. Liu, P. Zhou, An optoelectronic synapse based on two-dimensional violet phosphorus heterostructure, Adv. Sci. 10 (2023) 2301851.
[25] Y.-X. Hou, Y. Li, Z.-C. Zhang, J.-Q. Li, D.-H. Qi, X.-D. Chen, J.-J. Wang, B.-W. Yao, M.-X. Yu, T.-B. Lu, J. Zhang, Large-scale and flexible optical synapses for neuromorphic computing and integrated visible information sensing memory processing, ACS Nano 15 (2020) 1497–1508.
[26] Y. Chen, X. Wang, L. Huang, X. Wang, W. Jiang, Z. Wang, P. Wang, B. Wu, T. Lin, H. Shen, Z. Wei, W. Hu, X. Meng, J. Chu, J. Wang, Ferroelectric-tuned van der Waals heterojunction with band alignment evolution, Nat. Commun. 12 (2021) 4030.
[27] Y. Jiang, L. Zhang, R. Wang, H. Li, L. Li, S. Zhang, X. Li, J. Su, X. Song, C. Xia, Asymmetric ferroelectric-gated two-dimensional transistor integrating self-rectifying photoelectric memory and artificial synapse, ACS Nano 16 (2022) 11218–11226.
[28] K. Xu, B. Peng, H. Mao, Z. Wang, H. Gong, C. Fu, F.-F. Ren, Y. Yang, C. Wan, Q. Wan, J. Ye, Ga_2O_3 bipolar heterojunction-based optoelectronic synapse array with visual attention, J. Phys. Chem. Lett. 15 (2024) 556–564.
[29] X. Ji, B.D. Paulsen, G.K.K. Chik, R. Wu, Y. Yin, P.K.L. Chan, J. Rivnay, Mimicking associative learning using an ion-trapping non-volatile synaptic organic electrochemical transistor, Nat. Commun. 12 (2021) 2480.
[30] V.I. Govardovskii, P.D. Calvert, V.Y. Arshavsky, Photoreceptor light adaptation: untangling desensitization and sensitization, J. Gen. Physiol. 116 (2000) 791–794.
[31] M. Zhang, Z. Chi, G. Wang, Z. Fan, H. Wu, P. Yang, J. Yang, P. Yan, Z. Sun, An irradiance-adaptable near-infrared vertical heterojunction phototransistor, Adv. Mater. 34 (2022) 2205679.
[32] S.M. Kwon, S.W. Cho, M. Kim, J.S. Heo, Y.H. Kim, S.K. Park, Environment-adaptable artificial visual perception behaviors using a light-adjustable optoelectronic neuromorphic device array, Adv. Mater. 31 (2019) 1906433.
[33] M.H. Chiu, X. Ji, T. Zhang, N. Mao, Y. Luo, C. Shi, X. Zheng, H. Liu, Y. Han, W. L. Wilson, Z. Luo, V. Tung, J. Kong, Growth of large-sized 2D ultrathin SnSe crystals with in-plane ferroelectricity, Adv. Electron. Mater. 9 (2023) 202201031.
[34] L. Li, Z. Chen, Y. Hu, X. Wang, T. Zhang, W. Chen, Q. Wang, Single-layer single-crystalline SnSe nanosheets, J. Am. Chem. Soc. 135 (2013) 1213–1216.
[35] X.L. Shi, X. Tao, J. Zou, Z.G. Chen, High-performance thermoelectric SnSe: aqueous synthesis, innovations, and challenges, Adv. Sci. 7 (2020) 1902923.
[36] L. Xie, D. He, J. He, SnSe, the rising star thermoelectric material: a new paradigm in atomic blocks, building intriguing physical properties, Mater. Horiz. 8 (2021) 1847–1865.
[37] I. Grimaldi, T. Gerace, M.M. Pipita, I.D. Perrotta, F. Ciuchi, H. Berger, M. Papagno, M. Castriota, D. Pacilé, Structural investigation of InSe layered semiconductors, Solid State Commun. 311 (2020) 113855.
[38] C.-H. Wu, Y.-C. Huang, Y.-T. Ho, S.-J. Chang, S.-K. Wu, C.-H. Huang, W.-C. Chou, C.-S. Yang, Solid phase epitaxy of single phase two-dimensional layered InSe grown by MBE, Nanomaterials 12 (2022) 2435.
[39] Z. Zhang, Y. Yuan, W. Zhou, C. Chen, S. Yuan, H. Zeng, Y.-S. Fu, W. Zhang, Strain-induced bandgap enhancement of InSe ultrathin films with self-formed two-dimensional electron gas, ACS Nano 15 (2021) 10700–10709.
[40] F. Sui, M. Jin, Y. Zhang, R. Qi, Y.-N. Wu, R. Huang, F. Yue, J. Chu, Sliding ferroelectricity in van der Waals layered γ-InSe semiconductor, Nat. Commun. 14 (2023) 36.
[41] Y. Li, M. Che, N. Zhang, Y. Zou, X. Zhao, Y. Lin, B. Lv, X. Ma, Y. Shi, J. Yang, X. Sun, S. Li, D. Li, High-performance photodetector based on Bi2Se3/GeSe heterojunction with band alignment evolution, Adv. Opt. Mater. 12 (2023) 2302339.
[42] Z. Wang, H. Zhang, W. Wang, C. Tan, J. Chen, S. Yin, H. Zhang, A. Zhu, G. Li, Y. Du, S. Wang, F. Liu, L. Li, Type-I heterostructure based on WS2/PtS2 for high-performance photodetectors, ACS Appl. Mater. Interfaces 14 (2022) 37926–37936.
[43] J. Shang, L. Pan, X. Wang, J. Li, H.-X. Deng, Z. Wei, Tunable electronic and optical properties of InSe/InTe van der Waals heterostructures toward optoelectronic applications, J. Mater. Chem. C. 6 (2018) 7201–7206.
[44] T. Yamaoka, H.E. Lim, S. Koirala, X. Wang, K. Shinokita, M. Maruyama, S. Okada, Y. Miyauchi, K. Matsuda, Efficient photocarrier transfer and effective photoluminescence enhancement in type I monolayer MoTe2/WSe2 heterostructure, Adv. Funct. Mater. 28 (2018) 1801021.

[45] Y.H. Zhou, Z.B. Zhang, P. Xu, H. Zhang, B. Wang, UV-Visible photodetector based on I-type heterostructure of ZnO-QDs/Monolayer MoS_2, Nanoscale Res. Lett. 14 (2019) 364.
[46] R. Liu, F. Wang, L. Liu, X. He, J. Chen, Y. Li, T. Zhai, Band alignment engineering in two-dimensional transition metal dichalcogenide-based heterostructures for photodetectors, Small Struct. 2 (2020) 2000136.
[47] C.-H. Lee, G.-H. Lee, A.M. van der Zande, W. Chen, Y. Li, M. Han, X. Cui, G. Arefe, C. Nuckolls, T.F. Heinz, J. Guo, J. Hone, P. Kim, Atomically thin p–n junctions with van der Waals heterointerfaces, Nat. Nanotechnol. 9 (2014) 676–681.
[48] Y. Yan, G. Abbas, F. Li, Y. Li, B. Zheng, H. Wang, F. Liu, Self-driven high performance broadband photodetector based on SnSe/InSe van der Waals heterojunction, Adv. Mater. Interfaces 9 (2022) 2102068.
[49] Z. Liu, K. Ding, Z. Liu, F. Zhang, H. Zeng, K. Xu, Y. Sun, D. Wang, Y. Li, Kinetics-driven one-dimensional growth of van der Waals layered SnSe, J. Phys. Chem. C. 125 (2021) 12730–12737.
[50] S.-W. Hsiao, C.-S. Yang, H.-N. Yang, C.-H. Wu, S.-K. Wu, L.-Y. Chang, Y.-T. Ho, S.-J. Chang, W.-C. Chou, Novel method for the growth of two-dimensional layered InSe thin films on amorphous substrate by Molecular Beam Epitaxy, Front. Mater. 9 (2022) 871003.
[51] S. Liu, Y. Chen, S. Yang, C. Jiang, SnSe field-effect transistors with improved electrical properties, Nano Res 15 (2021) 1532–1537.
[52] R. Zhuo, L. Zeng, H. Yuan, D. Wu, Y. Wang, Z. Shi, T. Xu, Y. Tian, X. Li, Y.H. Tsang, In-situ fabrication of PtSe2/GaN heterojunction for self-powered deep ultraviolet photodetector with ultrahigh current on/off ratio and detectivity, Nano Res 12 (2018) 183–189.
[53] Y. Pan, R. Guzman, S. Li, W. Xu, Y. Li, N. Tang, H. Yin, J. He, A. Wu, J. Chen, W. Zhou, X. Xu, Y. Ye, Heteroepitaxy of semiconducting 2H-MoTe2 thin films on arbitrary surfaces for large-scale heterogeneous integration, Nat. Synth. 1 (2022) 701–708.
[54] W. Chen, R. Liang, S. Zhang, Y. Liu, W. Cheng, C. Sun, J. Xu, Ultrahigh sensitive near-infrared photodetectors based on MoTe2/germanium heterostructure, Nano Res 13 (2019) 127–132.
[55] C. Kim, T.J. Yoo, K.E. Chang, M.G. Kwon, H.J. Hwang, B.H. Lee, Highly responsive near-infrared photodetector with low dark current using graphene/germanium Schottky junction with Al_2O_3 interfacial layer, Nanophotonics 10 (2021) 1573–1579.
[56] X. Liu, F. Li, M. Xu, J. Qi, Self-powered, high response and fast response speed metal–insulator–semiconductor structured photodetector based on 2D MoS_2, RSC Adv. 8 (2018) 28041–28047.
[57] B.G. Singidas, A.E. De los Reyes, H.R. Bardolaza, J.D.E. Vasquez, A.A. Salvador, E. S. Estacio, R.V. Sarmago, Graphene transfer passivates GaAs, Appl. Phys. Lett. 117 (2020) 171105.
[58] W. Seo, W. Park, H.Y. Seo, S. Oh, O. Kwon, S.H. Jeong, D.H. Kim, M.J. Kim, S. K. Lee, B.H. Lee, B. Cho, MoS2/p-Si heterojunction with graphene interfacial layer for high performance 940 nm infrared photodetector, Appl. Surf. Sci. 604 (2022) 154485.
[59] H. Wang, Z. Li, D. Li, P. Chen, L. Pi, X. Zhou, T. Zhai, Van der Waals integration based on two-dimensional materials for high-performance infrared photodetectors, Adv. Funct. Mater. 31 (2021) 2103106.
[60] Z. Lu, Y. Xu, Y. Yu, K. Xu, J. Mao, G. Xu, Y. Ma, D. Wu, J. Jie, Ultrahigh speed and broadband few-layer MoTe2/Si 2D–3D heterojunction-based photodiodes fabricated by pulsed laser deposition, Adv. Funct. Mater. 30 (2020) 1907951.
[61] J. Lee, N.T. Duong, S. Bang, C. Park, D.A. Nguyen, H. Jeon, J. Jang, H.M. Oh, M. S. Jeong, Modulation of junction modes in SnSe2/MoTe2 broken-gap van der Waals heterostructure for multifunctional devices, Nano Lett. 20 (2020) 2370–2377.
[62] W. Chen, R. Liang, S. Zhang, Y. Liu, W. Cheng, C. Sun, J. Xu, Ultrahigh sensitive near-infrared photodetectors based on MoTe2/germanium heterostructure, Nano Res 13 (2019) 127–132.
[63] H. Wang, Y. Zeng, F. Meng, R. Cao, Y. Liu, Z. Guo, T. Wang, H. Hu, S. Fan, Y. Yang, S. Wageh, O.A. Al-Hartomy, A. Kalam, Y. Shao, Y.-J. Zeng, D. Fan, H. Zhang, Interlayer sensitized van der Waals heterojunction photodetector with enhanced performance, Nano Res 16 (2023) 10537–10544.
[64] K. Patel, G. Solanki, K. Patel, V. Pathak, P. Chauhan, Investigation of optical, electrical and optoelectronic properties of SnSe crystals, Eur. Phys. J. B 92 (2019) 200.
[65] Y. Chen, X. Wang, G. Wu, Z. Wang, H. Fang, T. Lin, S. Sun, H. Shen, W. Hu, J. Wang, J. Sun, X. Meng, J. Chu, High-performance photovoltaic detector based on MoTe2/MoS2 Van der Waals heterostructure, Small 14 (2018) 1703293.
[66] J. Yao, Z. Zheng, G. Yang, All-Layered 2D Optoelectronics: A high-performance UV–vis–NIR broadband SnSe photodetector with Bi2Te3 topological insulator electrodes, Adv. Funct. Mater. 27 (2017) 1701823.
[67] V. Adinolfi, I.J. Kramer, A.J. Labelle, B.R. Sutherland, S. Hoogland, E.H. Sargent, Photojunction field-effect transistor based on a colloidal quantum dot absorber channel layer, ACS Nano 9 (2015) 356–362.
[68] J. Zhang, P. Guo, Z. Guo, L. Li, T. Sun, D. Liu, L. Tian, G. Zu, L. Xiong, J. Zhang, J. Huang, Retina-inspired artificial synapses with ultraviolet to near-infrared broadband responses for energy-efficient neuromorphic visual systems, Adv. Funct. Mater. 33 (2023) 2302885.
[69] H. Tan, Z. Ni, W. Peng, S. Du, X. Liu, S. Zhao, W. Li, Z. Ye, M. Xu, Y. Xu, X. Pi, D. Yang, Broadband optoelectronic synaptic devices based on silicon nanocrystals for neuromorphic computing, Nano Energy 52 (2018) 422–430.
[70] C. Lv, F. Zhang, C. Li, Z. Li, J. Zhao, Low-dimensional optoelectronic synaptic devices for neuromorphic vision sensors, Mater. Futures 2 (3) (2023).
[71] U. Sulutvedt, D. Zavagno, J. Lubell, S. Leknes, S.A. de Rodez Benavent, B. Laeng, Brightness perception changes related to pupil size, Vis. Res 178 (2021) 41–47.
[72] X. Huang, Y. Liu, G. Liu, K. Liu, X. Wei, M. Zhu, W. Wen, Z. Zhao, Y. Guo, Y. Liu, Short-wave infrared synaptic phototransistor with ambient light adaptability for flexible artificial night visual system, Adv. Funct. Mater. 33 (2022) 2208836.

Yinuo Zhang obtained her B.S. from Xi'an University of Technology in 2020. She is currently pursuing her Ph.D. degree at Xi'an Jiaotong University. Her research focuses on the 2D materials synthesis and interfacial engineering of heterojunctions for novel electronic devices.

Lan Li obtained her B.S. from University of Science and Technology Beijing in 2018. She is currently pursuing her M.S. degree at Xi'an Jiaotong University. Her research focuses on novel memristors based on atomic bi-stable structures.

Yunan Lin obtained his B. S. from Xi'an Jiaotong University. He's pursuing his M.S. degree at the same place. His research focuses on the surface modification and performance optimization of artificial synapses based on 2D materials.

Xuecen Miao obtained her M.S. degree from Xi'an Jiaotong University. During her master's studies, she participated in building a physical vapor deposition platform and developing neuromorphic devices. She is currently an engineer in optoelectronic device designing.

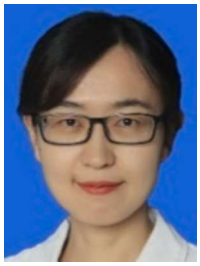

Hong Lei is a research associate at Shaanxi Institute for Pediatric Diseases, Xi'an Children's Hospital, affiliated with Xi'an Jiaotong University. She received her Ph.D. in biology/immunology from Humboldt University of Berlin in 2014. Her current research focuses on liver immunology and medical applications of 2D materials.

Yi Pan received his Ph.D. from IOP, CAS in 2011. Then, he became a postdoctoral researcher at FHI and PDI in Germany. He received the professor position at Xi'an Jiaotong University in 2017. His research interest is establishing a UHV-based atomic precision manufacturing technique for sub-nanometer device applications.